Available online at www.sciencedirect.com
SCIENCE DIRECT®
Journal of Solid State Chemistry 177 (2004) 2023–2038
JOURNAL OF SOLID STATE CHEMISTRY
http://elsevier.com/locate/jssc

Phase relations, crystal chemistry, and dielectric properties in sections of the La_2O_3–CaO–MgO–TiO_2 system

T.A. Vanderah,[a,*] V.L Miller,[a] I. Levin,[a] S.M. Bell,[b] and T. Negas[b]

[a] National Institute of Standards and Technology, Materials Science and Engineering Laboratory, Ceramics Division, 100 Bureau Dr. Stop 8520, Gaithersburg, MD 20899, USA
[b] TCI Ceramics, Inc., Hagerstown, MD 21742, USA

Received 13 October 2003; received in revised form 23 January 2004; accepted 1 February 2004

Abstract

Subsolidus phase equilibria and crystal chemistry were studied for the La_2O_3–MgO–TiO_2 system and for the ternary sections $LaMg_{1/2}Ti_{1/2}O_3$–$CaTiO_3$–La_2O_3 and $LaMg_{1/2}Ti_{1/2}O_3$–$CaTiO_3$–$La_{0.833}Mg_{0.25}Ti_{0.75}O_3$ in the quaternary La_2O_3–CaO–MgO–TiO_2 system. Dielectric properties (relative permittivity and temperature coefficient of resonant frequency, τ_f) were measured at 5–10 GHz and mapped onto the phase equilibria relations to reveal the compositions of temperature-stable ($\tau_f = 0$) compounds and mixtures. Phase equilibria relations were obtained by X-ray powder diffraction analysis of approximately 80 specimens prepared by solid-state reactions in air at ~1450°C. Six ternary phases were found to form in the La_2O_3–MgO–TiO_2 system, including the three previously reported compounds $LaMg_{1/2}Ti_{1/2}O_3$, $La_5Mg_{0.5}Ti_{3.5}O_{15}$, and "$La_6MgTi_4O_{18}$"; and the new phases $La_{10}MgTi_9O_{34}$, $La_9Mg_{0.5}Ti_{8.5}O_{31}$, and a perovskite-type solid solution $(1-x)LaMg_{1/2}Ti_{1/2}O_3$–$xLa_{2/3}TiO_3$ ($0 \leqslant x \leqslant 0.5$). The phase previously reported as "$La_6MgTi_4O_{18}$" was found to form off-composition, apparently as a point compound, at $La_6Mg_{0.913}Ti_{4.04}O_{18}$. Indexed experimental X-ray powder diffraction patterns are given for $LaMg_{1/2}Ti_{1/2}O_3$, $La_5Mg_{0.5}Ti_{3.5}O_{15}$, $La_6Mg_{0.913}Ti_{4.04}O_{18}$, $La_{10}MgTi_9O_{34}$, and $La_9Mg_{0.5}Ti_{8.5}O_{31}$. $LaMg_{1/2}Ti_{1/2}O_3$ exhibits a slightly distorted perovskite structure with ordered *B*-cations ($P2_1/n$; $a = 5.5608(2)$ Å, $b = 5.5749(3)$ Å, $c = 7.8610(5)$ Å, $\beta = 90.034(4)°$). $La_5Mg_{0.5}Ti_{3.5}O_{15}$ ($P\bar{3}m1$; $a = 5.5639(1)$, $c = 10.9928(5)$ Å) and $La_6Mg_{0.913}Ti_{4.04}O_{18}$ ($R3m$; $a = 5.5665(1)$, $c = 39.7354(9)$ Å) are $n = 5$ and $n = 6$ members, respectively, of the (111) perovskite-slab series $A_nB_{n-1}O_{3n}$. The new phases $La_{10}MgTi_9O_{34}$ ($a = 5.5411(2)$, $b = 31.3039(9)$, $c = 3.9167(1)$ Å) and $La_9Mg_{0.5}Ti_{8.5}O_{31}$ ($a = 5.5431(2)$, $b = 57.055(1)$, $c = 3.9123(1)$ Å) are $n = 5$ and $n = 4.5$ members, respectively, of the (110) perovskite-slab series $A_nB_nO_{3n+2}$, which exhibit orthorhombic subcells; electron diffraction revealed monoclinic superlattices with doubled *c*-parameters for both compounds. Extensive perovskite-type solid solutions form in the ternary sections $LaMg_{1/2}Ti_{1/2}O_3$–$CaTiO_3$–La_2O_3 and $LaMg_{1/2}Ti_{1/2}O_3$–$CaTiO_3$–$La_{0.833}Mg_{0.25}Ti_{0.75}O_3$. The La_2O_3–MgO–TiO_2 system contains two regions of temperature-stable ($\tau_f = 0$) compositions. The quaternary La_2O_3–CaO–MgO–TiO_2 system contains an extensive single-phase perovskite-type volume through which passes a surface of temperature-stable compositions with permittivities projected to be in the 40–50 range. Traces of this surface occur as lines of $\tau_f = 0$ perovskite-type phases in the ternary sections $LaMg_{1/2}Ti_{1/2}O_3$–$CaTiO_3$–La_2O_3 and $LaMg_{1/2}Ti_{1/2}O_3$–$CaTiO_3$–$La_{0.833}Mg_{0.25}Ti_{0.75}O_3$.
Published by Elsevier Inc.

Keywords: La_2O_3–MgO–TiO_2; $LaMg_{1/2}Ti_{1/2}O_3$–$CaTiO_3$–La_2O_3; La_2O_3–CaO–MgO–TiO_2; Lanthanum magnesium titanates; La_2MgTiO_6; Dielectric properties; Temperature-stable dielectrics

1. Introduction

Complex titanates, niobates, and tantalates display dielectric properties rendering them useful in communication systems as enabling components such as resonators and filters [1–6]. These ceramics are referred to as "microwave dielectrics", and include numerous perovskite-related ABO_3-type phases which exhibit dielectric properties strongly affected by *A*- and/or *B*-site cation substitution and/or ordering [7]. The present study was motivated by the perovskite-like solid solution occurring in the quaternary La_2O_3–CaO–MgO–TiO_2 system between $LaMg_{1/2}Ti_{1/2}O_3$ and $CaTiO_3$. The dielectric properties of the endmembers are markedly different: $LaMg_{1/2}Ti_{1/2}O_3$ exhibits a permittivity (ε) of 33 with a temperature coefficient of resonant frequency (τ_f) of −90 ppm/°C [3], whereas the

*Corresponding author. Fax: +1-301-975-5334.
E-mail address: terrell.vanderah@nist.gov (T.A. Vanderah).

0022-4596/$ - see front matter Published by Elsevier Inc.
doi:10.1016/j.jssc.2004.02.005

permittivity of $CaTiO_3$ is much higher (180) with a τ_f of opposite sign (+800 ppm/°C) [7,8]. A complete solid solution forms between them, and temperature-stability ($\tau_f = 0$) is achieved at 44:56 $LaMg_{1/2}Ti_{1/2}O_3$:$CaTiO_3$ with a permittivity of 48 [3]. Permittivities higher than 50 (and small positive τ_f values) are obtained with $CaTiO_3$ concentrations above 59 mol%, rendering the system of interest as a low-cost ceramic for 900 MHz applications. The present study was carried out to elucidate the subsolidus phase equilibria about the $LaMg_{1/2}Ti_{1/2}O_3$:$CaTiO_3$ solid solution in order to provide information that could be used to tailor its dielectric properties through the preparation of thermodynamically stable mixtures. The primary focus was determination of phase relations in the La_2O_3–MgO–TiO_2 system, which was the least-studied ternary subsystem, as well as phase equilibria involving the endmembers $LaMg_{1/2}Ti_{1/2}O_3$ and $CaTiO_3$.

1.1. Overview of the subsystems and previous work

Three compounds form in the **MgO–TiO_2** system: Mg_2TiO_4 (inverse spinel-type), $MgTiO_3$ (Geikielite, ilmenite-type) and $MgTi_2O_5$ (pseudobrookite-type).[1] Several reports have indicated that no binary compounds form in the **MgO–La_2O_3** system (see footnote 1). The binary **La_2O_3–TiO_2** system is more complex (see footnote 1). Early studies indicated the formation of three compounds: La_2TiO_5, $La_2Ti_2O_7$, and $La_4Ti_9O_{24}$ [9]. A later study reported a fourth compound, $La_4Ti_3O_{12}$, which forms with a perovskite-derived 12-layer hexagonal crystal structure, and which decomposes above 1450°C to La_2TiO_5 and $La_2Ti_2O_7$ [10–12]. The structure of La_2TiO_5 features Ti^{4+} in five-fold trigonal bypyramidal coordination [13], whereas $La_2Ti_2O_7$ adopts a perovskite-slab type structure [14,15]. $La_4Ti_9O_{24}$ [16] was confirmed to be isostructural with $Nd_4Ti_9O_{24}$ [17,18], which exhibits an orthorhombic framework-type structure featuring pairs of edge-sharing [TiO_6] octahedra with six- and eight-fold coordinated Nd^{3+}. A fifth compound, cation-deficient perovskite-related "$La_{2/3}TiO_3$" [19], does not occur as such in the La_2O_3–TiO_2 system, but is stabilized by small amounts of Ti^{3+}, by partial filling of the *A*-sites with mono- or divalent cations [12], or by partial substitution of Ti^{4+} with trivalent cations [3,20].

Three compounds have been reported to form in the ternary **La_2O_3–MgO–TiO_2** system: $LaMg_{1/2}Ti_{1/2}O_3$, $La_5Mg_{0.5}Ti_{3.5}O_{15}$, and $La_6MgTi_4O_{18}$ [11,21,22]. Perovskite-like $LaMg_{1/2}Ti_{1/2}O_3$ has been variously described as cubic, orthorhombic, or monoclinic [21,23]; however, a recent Rietveld analysis of X-ray powder diffraction data confirms monoclinic symmetry [23] with near-complete ordering of Mg^{2+} and Ti^{4+} on the *B*-sites, analogous to $NdMg_{1/2}Ti_{1/2}O_3$ [24]. $La_5Mg_{0.5}Ti_{3.5}O_{15}$ and $La_6MgTi_4O_{18}$ were reported as $n = 5$ and $n = 6$ members of the hexagonal homologous series $A_nB_{n-1}O_{3n}$ [11,22]. These structures feature perovskite-type slabs (with thickness $n - 1$ [BO_6] octahedra) extending parallel to $(111)_{perov}$, and separated by a layer of ordered *B*-cation vacancies. A study of phase relations in the La_2O_3–MgO–TiO_2 system at 1200°C [25] confirmed the formation of these three compounds; however, a large single-phase solid solution was reported about $LaMg_{1/2}Ti_{1/2}O_3$ suggesting extensive dissolution of $MgTiO_3$, which would apparently require the unusual substitution of Mg^{2+} on the *A*-sites of the perovskite structure.

A study of phase relations in the **CaO–MgO–TiO_2** system reported no ternary compound formation (see footnote 1) [26]. The **CaO–MgO–La_2O_3** system has apparently not been studied, but extensive compound formation would not be expected since no compounds (except solid solutions of the components) have been reported to form along each of the binaries (see footnote 1). In the **La_2O_3–CaO–TiO_2** system a number of compounds have been reported as well as equilibria involving $CaTiO_3$. Along the composition line $La_4Ti_3O_{12}$–$CaTiO_3$, the compounds $La_4CaTi_4O_{15}$ and $La_4Ca_2Ti_5O_{18}$ were reported to form [11,22,27,28] as $n = 5$ and $n = 6$ members of the hexagonal, perovskite-slab homologous series $A_nB_{n-1}O_{3n}$. These compounds are analogous to $La_5Mg_{0.5}Ti_{3.5}O_{15}$ and $La_6MgTi_4O_{18}$, respectively, mentioned above. Three other compounds along the composition line $La_2Ti_2O_7$–$CaTiO_3$ have been reported and characterized: $La_8CaTi_9O_{31}$, $La_4CaTi_5O_{17}$, and $La_4Ca_2Ti_6O_{20}$ [15,28–33]. These phases are $n = 4.5$, $n = 5$, and $n = 6$ members, respectively, of the perovskite-related series $A_nB_nO_{3n+2}$, which feature crystal structures built from perovskite-type slabs that extend parallel to the $(110)_{perov}$ planes. $CaTiO_3$ forms an extensive solid solution $(1-x)CaTiO_3$–$xLa_{2/3}TiO_3$, with *x*-values as high as 0.96 (see footnote 1) [34–36]. $CaTiO_3$ was also reported to dissolve up to 40 mol% La_2O_3 [37], resulting in the perovskite-related end-member $La_4Ca_3Ti_3O_{15}$. A recent study has characterized the details of cation ordering, symmetry changes, and dielectric properties that occur in this solid solution [38].

2. Experimental methods

Approximately 80 polycrystalline specimens (3–4 g each) were prepared by solid-state reactions using La_2O_3 (99.99%, dried at 850°C immediately prior to weighing), $CaCO_3$ (99.99%), $MgCO_3$ (high-purity, pre-analyzed by thermogravimetric analysis) and TiO_2 (phosphate-free).

[1] Phase Equilibria Diagrams (formerly Phase Diagrams for Ceramists), The American Ceramic Society, Westerville, OH. Figs. 11:9310, 2:2373, 6:6753, 1:716, 3:4572, Zr:316–7, 92–003, 11:9247, 3:4336, 1:69–70, 4:5380, 4:5142, 12:10052, 12:9896, 3:4312.

Prior to each heat treatment, samples were ground with an agate mortar and pestle for 15 min, pelletized, and placed on sacrificial powder of the same composition on Pt foil supported by alumina ceramic. After an initial overnight calcine at 950°C, multiple 2–7 d heatings (with intermediate grinding and re-pelletizing) were carried out at ~1450°C. Samples were furnace-cooled to ~700°C and then air-quenched on the bench-top. Typically, four to five heatings were required to attain equilibrium, which was presumed when no further changes could be detected in the weakest peaks observed in the X-ray powder diffraction patterns. In the La_2O_3–MgO–TiO_2 system, minima in the solidus temperatures were observed at 1460°C and 1470°C near the compositions 0.4048:0.0119:0.5833 and 0.2000:0.3200:0.4800 molar ratios $\frac{1}{2}La_2O_3$:MgO:TiO_2, respectively.

Phase assemblages were ascertained using X-ray powder diffraction data, obtained with a Philips[2] diffractometer equipped with incident Soller slits, theta-compensating slit and a graphite monochromator, and a scintillation detector. Samples were mounted in welled glass slides. Patterns were collected at ambient temperatures using Cu$K\alpha$ radiation with a 0.02° 2θ step size and a 2 s count time; longer scans (0.015° step, 4 s count) were carried out to obtain data for least-squares refinement of lattice parameters. Intensity data measured as relative peak heights above background of hand-picked peaks were obtained using the Siemens DIFFRAC5000 second derivative peak locate program. The observed 2θ line positions reported here have been corrected using SRM 660, LaB_6 [39], as an external calibrant. Lattice parameters were refined using the corrected powder diffraction data (2θ values, Cu$K\alpha_1 = 1.540562$ Å) with the least-squares program CELLSVD [40]. Figures of merit (F_N) for indexed powder patterns were calculated according to Ref. [41]. The GSAS package [42] was used to calculate powder patterns from single-crystal data. Selected specimens were analyzed using transmission electron microscopy. The TEM specimens were prepared by conventional polishing, dimpling, and ion-thinning. The specimens were examined in a Philips EM 430 TEM operated at 200 kV.

Dielectric properties were measured at microwave frequencies using sintered pellets either ~8 or ~11 mm in diameter and ~5 mm high. Pellet densities (ρ_{obs}/ρ_{calc}) were determined geometrically. Measurements of the $TE_{01\delta}$ resonant mode were carried out using an HP 8720D Vector Network Analyzer and a gold-plated aluminum test cavity (~38 mm in diameter by ~25 mm high); unloaded quality factor Q (where $Q = 1/\tan\delta$; $\tan\delta$ = dielectric loss tangent) was measured at ambient temperature using the transmission method [43]. Relative permittivity (ε_{obs}) was calculated from the sample size and resonant frequency. The temperature coefficient of resonant frequency (τ_f) was measured for each sample between the two points of 25°C and 60°C using an environmental chamber. For samples with high dielectric loss (i.e., low quality factors and therefore very broad resonance signals), ε values were verified by capacitance measurements at 100 kHz using copper foil electrodes and a HP 4274A LCR meter. Permittivity values were corrected (ε_{corr}) to theoretical density using an effective-medium formalism [44]. The uncertainties in the corrected permittivity values are approximately ±3% and are dominated by the estimates of pore volume. The reproducibility of Q measurements was ±5%; the reproducibility of τ_f measurements was approximately ±2 ppm/°C.

[2] Certain commercial equipment is identified in order to adequately specify the experimental procedure; recommendation or endorsement by the National Institute of Standards and Technology is not therein implied.

3. Results and discussion

Subsolidus phase equilibria relations were determined for the La_2O_3–MgO–TiO_2 system (Figs. 1 and 2) and for two ternary sections in the quaternary La_2O_3–CaO–MgO–TiO_2 system: $LaMg_{1/2}Ti_{1/2}O_3$–$CaTiO_3$–La_2O_3 and $LaMg_{1/2}Ti_{1/2}O_3$–$CaTiO_3$–$La_{0.833}Mg_{0.25}Ti_{0.75}O_3$. All dielectric properties measured in the present study are collected in Table 1 and will be discussed in the corresponding sections below. The letter designations for compounds in Table 1 refer to the labels given in Fig. 2.

3.1. La_2O_3–MgO–TiO_2 system

The subsolidus phase equilibria relations found in the present study are shown in Fig. 1. Six ternary phases were found, as indicated in Fig. 2 (**A–F**), including an extensive solid solution along the composition line between $LaMg_{1/2}Ti_{1/2}O_3$ and $La_{2/3}TiO_3$ (**B**). The X-ray powder diffraction data for $LaMg_{1/2}Ti_{1/2}O_3$ (**A**) were indexed with a monoclinic unit cell (Table 2), in agreement with other work [23] and analogously to $NdMg_{1/2}Ti_{1/2}O_3$ [24]. The relative permittivity obtained for $LaMg_{1/2}Ti_{1/2}O_3$ was 27 and is within the range of values reported for this compound [23].

3.1.1. $La_n(Mg,Ti)_{n-1}O_{3n}$ (111) perovskite-slab compounds

Formation of the two previously reported $n = 5$ and $n = 6$ members [11,22,25] was confirmed. The $n = 5$ phase $La_5Mg_{0.5}Ti_{3.5}O_{15}$ (**C**) formed readily and apparently as a point compound. All peaks observed in the X-ray powder diffraction pattern could be indexed with a unit cell and space group analogous to that reported in

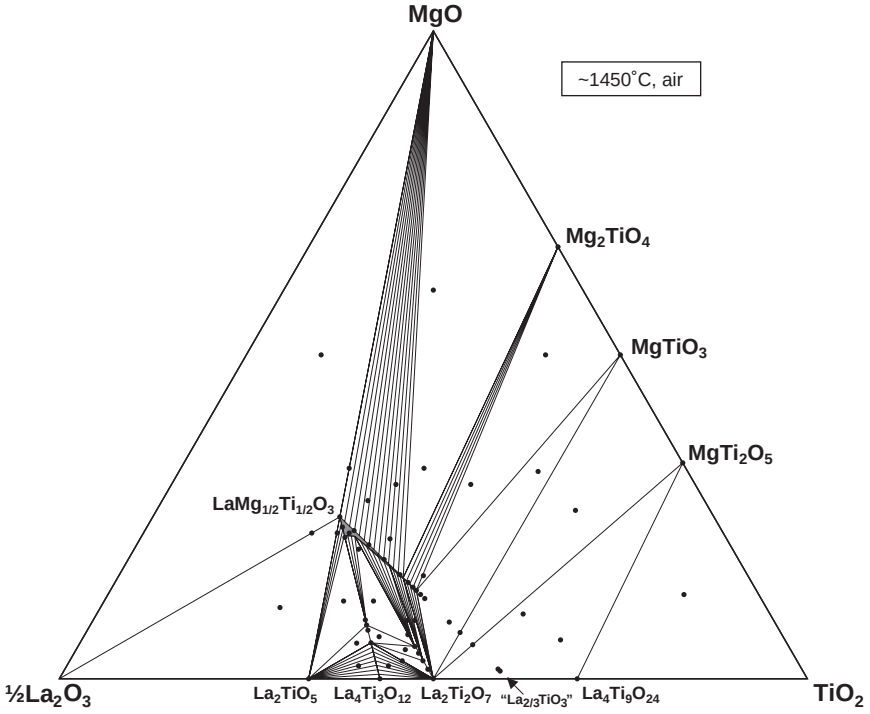

Fig. 1. Subsolidus phase equilibria relations determined for the La_2O_3–MgO–TiO_2 system from X-ray powder diffraction studies of specimens prepared in air at ~1450°C. Six ternary phases, including an extensive solid solution along the composition line between $LaMg_{1/2}Ti_{1/2}O_3$ and $La_{2/3}TiO_3$, were found to form.

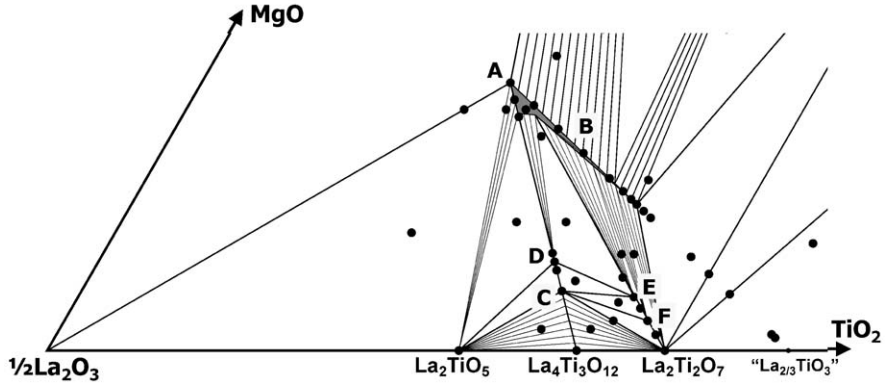

Fig. 2. Expanded region of the La_2O_3–MgO–TiO_2 system showing the ternary phases that form. **A** = perovskite-like $LaMg_{1/2}Ti_{1/2}O_3$, which forms the solid solution (**B**) $(1-x)LaMg_{1/2}Ti_{1/2}O_{3-x}La_{2/3}TiO_3$, $0.0 \leqslant x \leqslant 0.5$. As shown here, this solid solution "has width", and extends toward the La_2O_3–TiO_2 binary to form a narrow, perovskite-like single-phase region. Compounds **C** and **D** (along with $La_4Ti_3O_{12}$) are members of the hexagonal (or trigonal) defect-perovskite homologous series $A_nB_{n-1}O_{3n}$: **C** = $La_5Mg_{0.5}Ti_{3.5}O_{15}$ ($n = 5$), **D** = $La_6Mg_{0.913}Ti_{4.04}O_{18}$ ($n = 6$). **E** and **F** (along with $La_2Ti_2O_7 = La_4Ti_4O_{14}$) are members of the homologous series $A_nB_nO_{3n+2}$, which features slabs ($n[BO_6]$ octahedra thick) of the perovskite structure extending parallel to the perovskite (110) planes: **E** = $La_{10}MgTi_9O_{34}$ ($n = 5$), **F** = $La_9Mg_{0.5}Ti_{8.5}O_{31}$ ($n = 4.5$, alternating slab thicknesses of 4 and 5 octahedra).

a single-crystal study of $Ba_5Nb_4O_{15}$ [45]; the results are given in Table 3. The powder pattern calculated using the refined unit cell (Table 3), the positional parameters and space group for $Ba_5Nb_4O_{15}$ [45], and assuming disordered Mg^{2+} and Ti^{4+} on the *B*-sites matched the observed pattern, suggesting that $La_5Mg_{0.5}Ti_{3.5}O_{15}$ and $Ba_5Nb_4O_{15}$ are isostructural. In contrast, the $n = 6$ phase formed sluggishly with broad powder diffraction lines, and stoichiometric $La_6MgTi_4O_{18}$ specimens always contained small amounts of $LaMg_{1/2}Ti_{1/2}O_3$. Preparation of closely spaced compositions indicated that the $n = 6$ phase forms as a point compound at the cation-deficient stoichiometry $La_6Mg_{0.913}Ti_{4.04}\square_{0.047}O_{18}$ (**D**), which corresponds to 1% *B*-cation vacancies (□). Inspection of this sample by TEM found a highly defective sample with the dominant phase having the $n = 6$ type structure. X-ray powder diffraction data for a $La_6Mg_{0.913}Ti_{4.04}O_{18}$ sample annealed for 2 weeks at

Table 1
Dielectric properties of selected compounds found in the La_2O_3–CaO–MgO–TiO_2 system.

Compound	ρ_{obs}/ρ_{calc} (%)	ε_{Obs}	ε_{Corr}	τ_f (ppm/°C)	f (GHz)	Qxf (GHz)[a]
$(1-x)LaMg_{1/2}Ti_{1/2}O_3$:$xLa_{2/3}TiO_3$ solid solution (B, Fig. 2)						
$x=0$, $LaMg_{1/2}Ti_{1/2}O_3$ (**A**)	90	23	27	−82	7.0	60,000
$x=0.10$	97	28	29	−66	6.6	56,000
$x=0.20$	95	31	33	−54	6.3	43,000
$x=0.30$	94	33	36	−51	6.0	28,000
$x=0.40$	98	37	38	−46	5.6	3400
$x=0.45$	94	42	46	−30	4.8	4500
$x=0.48$	83	39	50	+23	4.6	3800
$x=0.50$	82	38	51	+23	4.6	3000
$La_n(Mg,Ti)_{n-1}O_{3n}$ (111) perovskite-slab series						
$La_4Ti_3O_{12}$, $n=4$	88	36	43	−39	5.8	26,000
$La_5Mg_{0.5}Ti_{3.5}O_{15}$, $n=5$ (**C**)	92	34	38	−16	6.0	31,000
$La_6Mg_{0.913}Ti_{4.04}O_{18}$, $n=6$ (**D**)	95	32	34	−46	6.1	31,000
$La_n(Mg,Ti)_nO_{3n+2}$ (110) perovskite-slab series						
$La_2Ti_2O_7$, $n=4$	95	43	46	−6	5.5	~2200
$La_9Mg_{0.5}Ti_{8.5}O_{31}$, $n=4.5$ (**F**)	87	42	51	−11	8.4	15,000
$La_{10}MgTi_9O_{34}$, $n=5$ (**E**)	89	29	34	−22	5.9	13,000
$La_{0.5-2a+2b}Ca_{0.5+2a-2b}[Ca_bMg_{0.25-a}Ti_{0.75+a-b}]O_3$ perovskites						
$La_{0.42}Ca_{0.58}[Ca_{0.05}Mg_{0.16}Ti_{0.79}]O_3$	98	38	39	+25	5.3	20,000
$La_{0.43}Ca_{0.57}[Ca_{0.08}Mg_{0.14}Ti_{0.78}]O_3$	95	42	45	+9	5.0	18,000
$La_{0.39}Ca_{0.61}[Ca_{0.11}Mg_{0.08}Ti_{0.81}]O_3$	95	46	50	+36	4.7	17,000
$La_{0.57}Ca_{0.43}[Ca_{0.11}Mg_{0.18}Ti_{0.71}]O_3$		43		−19	3.5	26,000
$La_{0.65}Ca_{0.35}[Ca_{0.25}Mg_{0.075}Ti_{0.675}]O_3$	90	26	30	−70	7.0	16,000

[a] No attempt was made to optimize Q-values.

1475°C are given in Table 4 and were indexed analogously to $Sr_6TiNb_4O_{18}$ [46]. The powder pattern calculated using the refined unit cell (Table 4), the positional parameters and space group reported in the single-crystal study of $Sr_6TiNb_4O_{18}$ [46], and assuming disordered Mg^{2+} and Ti^{4+} on the B-sites matched the observed pattern, suggesting that $La_6Mg_{0.913}Ti_{4.04}O_{18}$ and $Sr_6TiNb_4O_{18}$ are isostructural.

The crystal structures of $La_5Mg_{0.5}Ti_{3.5}O_{15}$ and $La_6Mg_{0.913}Ti_{4.04}O_{18}$ are shown in Fig. 3 [47]. As found for other $A_nB_{n-1}O_{3n}$ homologs, they display unit cells with similar a-parameters, and c-parameters that reflect the number of close-packed layers (here, at 2.2 Å/layer) in the unit cell (five for $n=5$ and eighteen for $n=6$). The solid solution indicated between $La_4Ti_3O_{12}$ ($n=4$) and $La_5Mg_{0.5}Ti_{3.5}O_{15}$ (**C**, $n=5$) (Figs. 1 and 2) likely occurs by the formation of intergrowths of the two structures.

3.1.2. $La_n(Mg,Ti)_nO_{3n+2}$ (110) perovskite-slab compounds

The present study found two phases, $La_{10}MgTi_9O_{34}$ (compound **E**) and $La_9Mg_{0.5}Ti_{8.5}O_{31}$ (compound **F**), which have not been previously reported. X-ray powder diffraction data for $La_{10}MgTi_9O_{34}$ are given in Table 5 and were indexed analogously to $Sr_5TiNb_4O_{17}$ [48]. The powder pattern calculated using the refined unit cell (Table 5), the positional parameters and space group reported in the single-crystal study of $Sr_5TiNb_4O_{17}$ [48], and assuming disordered Mg^{2+} and Ti^{4+} on the B-sites matched the observed pattern. These results suggest that $La_{10}MgTi_9O_{34}$ is an $n=5$ member of the (110) perovskite-slab homologous series $A_nB_nO_{3n+2}$, several of which have been found in the La_2O_3–CaO–TiO_2 [15,29–32] as well as other systems [48].

As shown in Fig. 4, the $A_nB_nO_{3n+2}$ structures consist of slabs of the distorted perovskite structure sliced parallel to the parent (110) perovskite planes, with n denoting the width of the slabs in number of [BO_6] octahedra. These homologs exhibit orthorhombic subcells with similar a- (~5.5 Å) and c- (~3.9 Å) parameters, and variable b-parameters that reflect slab thickness and translational symmetry—they are readily distinguished by characteristic diffraction lines below 15° 2θ. Many $A_nB_nO_{3n+2}$ structures feature sequences of reversible displacive phase transitions associated with cooperative rotations of the [BO_6] octahedra [49]. In particular, $La_2Ti_2O_7$ (=$La_4Ti_4O_{14}$, $n=4$) undergoes the following sequence of reversible tilting phase transitions on cooling [50]: $Amam \rightarrow A2_1am \rightarrow$ (incommensurate phase) $\rightarrow P2_1$. For this compound, the $Amam \rightarrow A2_1am$ transition is associated with in-phase rotation of octahedra about the c-axis, while the subsequent $A2_1am \rightarrow P2_1$ symmetry reduction (through

Table 2
X-ray powder diffraction data for La_2MgTiO_6 (**A**, Fig. 2), $P2_1/n$; $a = 5.5608(2)$, $b = 5.5749(3)$, $c = 7.8610(5)$ Å; $\beta = 90.034(4)^\circ$

h	k	l	$2\theta_{obs}$	I_{obs}	$2\theta_{calc}$	$\Delta 2\theta$	d_{obs}
0	1	1	19.503	2	19.505	−0.002	4.548
1	1	0	22.576	29	22.565	0.011	3.9352
1	1	1	25.276	3	25.283	−0.007	3.5206
−1	1	2	32.140	100	32.146	−0.006	2.7827
0	2	1	34.078	3	34.099	−0.021	2.6287
2	1	0	36.052	1	36.069	−0.017	2.4892
−2	1	1	37.888	3	37.892	−0.004	2.3727
−2	0	2	39.642	31	39.663	−0.021	2.2717
1	1	3	41.357	2	41.365	−0.008	2.1813
1	2	2	42.958	1	42.944	0.014	2.1037
2	2	0	46.072	38	46.071	0.001	1.9685
−2	2	1	47.567	6	47.575	−0.008	1.9100
−2	1	3	50.535	1	50.530	0.005	1.8046
3	1	0	51.941	15	51.944	−0.003	1.7590
1	3	1	53.203	6	53.220	−0.017	1.7202
0	2	4	57.317	43	57.315	0.002	1.6061
2	2	3	58.603	2	58.618	−0.015	1.5739
−1	2	4	59.881	1	59.883	−0.002	1.5433
−3	0	3	61.187	1	61.179	0.008	1.5135
−1	3	3	63.561	3	63.560	0.001	1.4626
−2	2	4	67.252	19	67.246	0.006	1.3910
0	4	1	68.281	2	68.292	−0.011	1.3725
0	2	5	68.455	1	68.458	−0.002	1.3694
4	1	1	70.827	1	70.824	0.003	1.3293
−3	1	4	71.966	7	71.967	−0.001	1.3110
3	3	1	73.023	2	73.042	−0.019	1.2946
4	2	0	76.526	14	76.511	0.015	1.2438
0	4	3	77.520	3	77.511	0.009	1.2304
−4	2	1	77.626	1	77.633	−0.007	1.2289
0	3	5	79.856	1	79.847	0.009	1.2001
4	2	2	81.012	5	81.015	−0.003	1.1859
−3	3	3	82.047	3	82.043	0.004	1.1735
0	4	4	85.321	4	85.306	0.015	1.1367
4	0	4	85.508	3	85.514	−0.006	1.1347
−2	4	3	86.396	2	86.391	0.005	1.1253
2	3	5	88.703	1	88.713	−0.010	1.1019
3	3	4	89.824	3	89.809	0.015	1.0910

Figure of merit: $F_{37} = 38.1$ (0.0084, 116) [41].

Table 3
X-ray powder diffraction data for $La_5Mg_{0.5}Ti_{3.5}O_{15}$ (**C**, Fig. 2) $n = 5$ member, $A_nB_{n-1}O_{3n}$ (111) perovskite-slab series $P3m1$; $a = 5.5639(1)$, $c = 10.9928(5)$ Å

h	k	l	$2\theta_{obs}$	I_{obs}	$2\theta_{calc}$	$\Delta 2\theta$	d_{obs}
1	0	0	18.394	1	18.398	−0.004	4.819
1	0	1	20.108	10	20.104	0.004	4.4123
1	0	2	24.527	13	24.549	−0.022	3.6264
1	0	3	30.640	100	30.626	0.014	2.9154
1	1	0	32.148	75	32.149	−0.001	2.7820
2	0	0	37.293	1	37.292	0.001	2.4092
1	0	4	37.640	1	37.649	−0.009	2.3878
2	0	1	38.223	11	38.211	0.012	2.3527
2	0	2	40.864	25	40.863	0.001	2.2065
0	0	5	40.995	31	41.018	−0.023	2.1998
2	0	3	45.007	57	44.994	0.013	2.0125
1	1	4	46.408	1	46.406	0.002	1.9550
2	0	4	50.303	1	50.325	−0.022	1.8124
2	1	1	50.771	1	50.772	−0.001	1.7968
2	1	2	52.924	12	52.919	0.005	1.7286
1	1	5	53.025	14	53.046	−0.021	1.7256
1	0	6	53.473	24	53.461	0.012	1.7122
2	1	3	56.367	41	56.369	−0.002	1.6309
3	0	0	57.295	23	57.316	−0.021	1.6067
1	1	6	60.457	1	60.452	0.005	1.5300
2	1	4	60.971	1	60.981	−0.010	1.5183
1	0	7	62.096	1	62.115	−0.019	1.4935
2	0	6	63.785	14	63.766	0.019	1.4579
2	1	5	66.650	1	66.626	0.024	1.4021
2	2	0	67.252	17	67.252	0.000	1.3909
1	0	8	71.333	6	71.313	0.020	1.3211
2	0	7	71.658	4	71.677	−0.019	1.3159
3	0	5	72.854	1	72.872	−0.018	1.2972
2	1	6	73.228	1	73.220	0.008	1.2915
3	1	3	75.689	15	75.689	0.000	1.2555
1	1	8	77.380	1	77.398	−0.018	1.2322
0	0	9	78.212	1	78.195	0.017	1.2212
2	0	8	80.373	1	80.382	−0.009	1.1937
2	2	5	81.877	1	81.884	−0.007	1.1756
4	0	3	84.615	1	84.615	0.000	1.1444
3	1	5	84.856	1	84.833	0.023	1.1417
1	1	9	87.078	1	87.063	0.015	1.1182
3	2	1	88.923	1	88.907	0.016	1.0997
2	1	8	89.216	1	89.213	0.003	1.0969

Figure of merit: $F_{39} = 46.1$ (0.0113, 75) [41].

the incommensurate phase) is caused by octahedral tilting about the long b-axis; the latter transition doubles the c-lattice parameter. A classification scheme that relates the stacking sequences of the {110} perovskite-like layers and octahedral tilt systems to the symmetry of the $A_nB_nO_{3n+2}$ structures has been reported previously [49].

Examination of single grains of the $n = 5$ compound $La_{10}MgTi_9O_{34}$ using electron diffraction indicated doubling of the c-parameter (Fig. 5), similar to that observed for the $La_2Ti_2O_7$. The resulting unit cell is monoclinic and the reflection conditions are consistent with the $P2_1/b11$ space group, which has been commonly reported for other $n = 5$ members of $A_nB_nO_{3n+2}$ series; i.e., $Sr_5Nb_5O_{17}$ and $Ca_5Nb_5O_{17}$. The unit cell and indexing in Table 5 therefore correspond to the orthorhombic subcell of $La_{10}MgTi_9O_{34}$, whereas the actual symmetry of this phase is monoclinic.

The second new compound, $La_9Mg_{0.5}Ti_{8.5}O_{31}$ (compound **F**), was found to occur between $La_{10}MgTi_9O_{34}$ ($n = 5$) and $La_2Ti_2O_7$ ($n = 4$). X-ray powder diffraction data for $La_9Mg_{0.5}Ti_{8.5}O_{31}$ are given in Table 6. All lines could be indexed with an orthorhombic unit cell analogous to the subcell for the "$n = 4.5$" $A_nB_nO_{3n+2}$ homolog in the $SrO–TiO_2–Nb_2O_5$ system [51], which features perovskite slabs alternately 4 and 5 octahedra in width—the long b-dimension of the unit cell is approximately equal to the sum of those for the $n = 4$ and $n = 5$ compounds. Again, electron diffraction confirmed the actual symmetry of $La_9Mg_{0.5}Ti_{8.5}O_{31}$ to be monoclinic with a doubled c-parameter compared to the orthorhombic subcell, as found for $La_{10}MgTi_9O_{34}$ and for other $n = 4.5$ homologs that form in the

Table 4
X-ray powder diffraction for $La_6Mg_{0.913}Ti_{4.04}O_{18}$ (**D**, Fig. 2) $n=6$ member, $A_nB_{n-1}O_{3n}$ (111) perovskite-slab series $R3m$; $a=5.5665(1)$, $c=39.7354(9)$ Å

h	k	l	$2\theta_{obs}$	I_{obs}	$2\theta_{calc}$	$\Delta 2\theta$	d_{obs}
1	0	1	18.538	1	18.525	0.013	4.782
0	1	2	18.920	1	18.927	−0.007	4.687
1	0	4	20.459	10	20.461	−0.002	4.3374
1	0	7	24.206	14	24.201	0.005	3.6738
0	1	8	25.734	2	25.732	0.002	3.4590
1	0	10	29.116	1	29.099	0.017	3.0644
0	1	11	30.911	100	30.908	0.003	2.8905
1	1	0	32.139	59	32.134	0.005	2.7828
0	0	15	33.829	4	33.809	0.020	2.6475
1	0	13	34.742	1	34.722	0.020	2.5800
0	1	14	36.731	2	36.714	0.017	2.4447
0	2	1	37.348	1	37.345	0.003	2.4057
2	0	2	37.553	1	37.558	−0.005	2.3931
1	1	9	38.210	4	38.193	0.017	2.3534
0	2	4	38.399	7	38.397	0.002	2.3423
2	0	5	39.027	1	39.017	0.010	2.3060
0	2	7	40.642	23	40.631	0.011	2.2180
0	0	18	40.849	86	40.844	0.005	2.2073
2	0	8	41.601	1	41.613	−0.012	2.1691
0	2	10	43.908	1	43.897	0.011	2.0603
2	0	11	45.193	50	45.186	0.007	2.0047
1	0	19	47.349	6	47.342	0.007	1.9183
0	0	21	48.050	3	48.044	0.006	1.8919
2	0	14	49.579	2	49.576	0.003	1.8371
1	2	2	50.224	1	50.242	−0.018	1.8150
2	1	4	50.908	2	50.911	−0.003	1.7922
2	1	7	52.714	7	52.719	−0.005	1.7350
0	2	16	52.881	13	52.890	−0.009	1.7299
1	2	8	53.538	1	53.526	0.012	1.7102
1	0	22	54.182	38	54.185	−0.003	1.6914
0	0	24	55.450	1	55.452	−0.002	1.6557
1	2	11	56.529	33	56.522	0.007	1.6266
3	0	0	57.290	16	57.287	0.003	1.6068
0	2	19	58.363	2	58.370	−0.007	1.5798
1	1	21	58.980	1	58.978	0.002	1.5647
1	2	14	60.314	1	60.314	0.000	1.5333
1	0	25	61.359	4	61.367	−0.008	1.5097
2	1	16	63.265	1	63.246	0.019	1.4687
0	2	22	64.411	15	64.406	0.005	1.4453
1	1	24	65.552	1	65.550	0.002	1.4229
2	2	0	67.213	12	67.217	−0.004	1.3917
2	1	19	68.214	1	68.208	0.006	1.3737
2	2	6	68.900	1	68.889	0.011	1.3617
0	2	25	70.983	4	70.973	0.010	1.3267
0	0	30	71.127	2	71.120	0.007	1.3244
0	1	29	71.522	8	71.527	−0.005	1.3181
1	3	7	72.567	3	72.581	−0.014	1.3016
3	0	18	72.706	6	72.727	−0.021	1.2995
2	1	22	73.807	14	73.812	−0.005	1.2828
3	1	11	75.803	12	75.804	−0.001	1.2539
0	2	28	78.078	1	78.082	−0.004	1.2229
0	0	33	79.539	7	79.541	−0.002	1.2041
4	0	4	80.139	2	80.156	−0.017	1.1966
2	0	29	80.569	5	80.580	−0.011	1.1913
1	3	16	81.720	5	81.734	−0.014	1.1774
0	4	11	84.716	6	84.719	−0.003	1.1433
1	1	33	88.365	13	88.376	−0.011	1.1052
0	0	36	88.515	10	88.513	0.002	1.1037
1	2	29	89.403	3	89.399	0.004	1.0951

Figure of merit: $F_{59}=70.3$ (0.0078, 107) [41].

$La_2Ti_2O_7$–$CaTiO_3$, $Nd_2Ti_2O_7$–$CaTiO_3$, and $Ca_2Nb_2O_7$–$CaTiO_3$ systems [15,29,30]. The reflection conditions for $La_9Mg_{0.5}Ti_{8.5}O_{31}$ were consistent with the space group $P2_1/b11$. The $n=6$ phase commonly found in other systems was not observed to form in the La_2O_3–MgO–TiO_2 system.

3.1.3. $(1-x)LaMg_{1/2}Ti_{1/2}O_3-xLa_{2/3}TiO_3$ solid solution

This solid solution forms by substitution of A-site vacancies for La^{3+} in $LaMg_{1/2}Ti_{1/2}O_3$ accompanied by an increase in the Ti^{4+}/Mg^{2+} ratio according to the formula $La_{1-x/3}\square_{x/3}[Mg_{(1-x)/2}Ti_{(1+x)/2}]O_3$, $0.0\leqslant x\leqslant 0.5$ (phase **B**, Fig. 2). Since Ti^{4+} is considerably smaller than Mg^{2+} (0.605 Å vs. 0.720 Å) [52], the cell volume decreases with increasing x-value, as seen in Fig. 6; however, the observed non-linearity suggests that the concurrent substitution of A-site vacancies has an opposing effect resulting in larger cell volumes than those expected from size effects alone. Other effects such as line splitting in the X-ray powder diffraction patterns indicate systematic changes in unit cell parameters with increasing x-value. The dielectric properties occurring in the solid solution are given in Table 1 and Fig. 7. In general, the relative permittivity increases and the temperature coefficient of resonant frequency (τ_f) becomes more positive with increasing x-value; τ_f changes sign near $x=0.47$. The data in Fig. 7 suggest a break in slope, with properties abruptly more sensitive to chemical composition above $x=0.4$. A detailed study of this solid solution using electron microscopy combined with variable-temperature X-ray powder diffraction and neutron powder diffraction revealed a sequence of displacive phase transitions associated with rotation of $[(Mg/Ti)O]_6$ octahedra; the transition temperatures decrease with increasing x. The extent of B-site ordering was observed to diminish with increasing x, and for $x>0.48$, short-range ordering of A-site vacancies was confirmed. The complete results of these studies will be described elsewhere.

As shown in Fig. 2, the $(1-x)LaMg_{1/2}Ti_{1/2}O_3-xLa_{2/3}TiO_3$ solid solution line was found to "have width"; i.e., it extends toward the (111) and (110) perovskite-slab compounds (**D** and **E**, respectively) to form a narrow single-phase region via the occurrence of B-site vacancies. $LaMg_{1/2}Ti_{1/2}O_3$ was found to dissolve ~18 mol% $La_6MgTi_4O_{18}$ (with endmembers expressed as $LaO_{1.5}$: MgO : TiO_2 mole fractions); essentially no shifts in the $LaMg_{1/2}Ti_{1/2}O_3$ lattice parameters were observed for specimens in this region.

3.1.4. Temperature-stable compositions in the La_2O_3–MgO–TiO_2 system

Dielectric properties are additive [53,54] and therefore assemblages of phases with both positive and negative temperature coefficients of resonant frequency (τ_f) must include temperature-stable ($\tau_f=0$) compositions. The

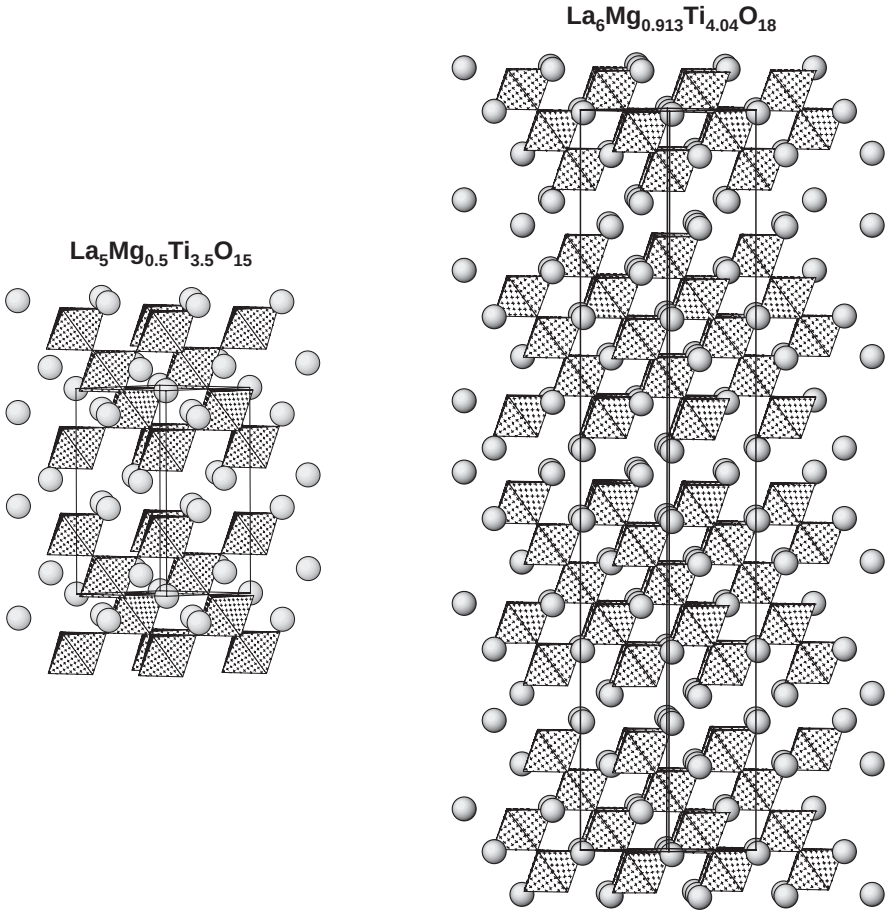

Fig. 3. Suggested crystal structures of trigonal $La_5Mg_{0.5}Ti_{3.5}O_{15}$ (compound **C**, Table 3) and rhombohedral $La_6Mg_{0.913}Ti_{4.04}O_{18}$ (compound **D**, Table 4) viewed along the ⟨110⟩ direction. The structures correspond to the $n = 5$ and $n = 6$ members, respectively, of the "(111) perovskite-slab" homologous series $A_nB_{n-1}O_{3n}$, with similar *a*-parameters, and *c*-parameters that reflect the number of close-packed layers in the unit cell (five for $n = 5$ and eighteen for $n = 6$). For reasons that are not understood, the $n = 6$ compound (**D**) does not form as a single phase at the ideal stoichiometry of $La_6MgTi_4O_{18}$; rather, it forms, with no observable solid solution, at the composition indicated, with 1% *B*-cation vacancies.

existence and approximate locations of these temperature-stable regions can be inferred by mapping the sign of τ_f onto the phase equilibria diagram, as shown in Fig. 8. (Data for the signs of τ_f were measured in the present study (Table 1) or were obtained from the literature and other sources [3,9,14,36,55,56]). The present data indicate that two $\tau_f = 0$ regions occur in the La_2O_3–MgO–TiO_2 system—one near TiO_2 (since τ_f changes sign between $MgTi_2O_5$ and TiO_2, and between $La_4Ti_9O_{24}$ and $La_2Ti_2O_7$), and another around the end of the $(1-x)LaMg_{1/2}Ti_{1/2}O_3$–$xLa_{2/3}TiO_3$ solid solution (for which τ_f becomes positive above $x = 0.47$), which is in equilibrium with compounds having negative τ_f values.

3.2. $LaMg_{1/2}Ti_{1/2}O_3$–$CaTiO_3$–La_2O_3 system

This ternary section in the quaternary La_2O_3–CaO–MgO–TiO_2 system features a large perovskite-related single-phase field bounded by the complete $LaMg_{1/2}Ti_{1/2}O_3-CaTiO_3$ solid solution and the partial solid solution of La_2O_3 in $CaTiO_3$, as shown in Fig. 9. In the present study it was found that $CaTiO_3$ dissolves up to 38 mol% La_2O_3, forming the solid solution $La_{2x}Ca_{1-2x}[Ca_xTi_{1-x}]O_3$, with a maximum *x*-value of 0.38 which corresponds to a limiting composition of $La_{0.76}Ca_{0.24}[Ca_{0.38}Ti_{0.62}]O_3$. The formation of this solid solution is likely facilitated by the propensity of the slightly smaller Ca^{2+} ions to occupy both the *A*- and *B*-sites of the perovskite structure. Earlier work reported that the composition $La_4Ca_3Ti_3O_{15}$ ($x = 0.40$) was single-phase [37]; however, in the present study this composition contained a small amount of La_2O_3 even after extensive re-heating at 1475°C.

Within the ternary section (Fig. 9) the composition of the perovskite-like phase can be expressed as $La_{0.5-2a+2b}Ca_{0.5+2a-2b}[Ca_bMg_{0.25-a}Ti_{0.75+a-b}]O_3$, which assumes that cation sites are fully occupied with the larger La^{3+} ions located in the *A*-sites and with Ca^{2+} ions occupying

Table 5
X-ray powder diffraction data for $La_{10}MgTi_9O_{34}$ (**E**, Fig. 2) $n=5$ member, $A_nB_nO_{3n+2}$ (110) perovskite-slab series; indexed with subcell *Pnnm*; $a=5.5411(2)$, $b=31.3039(9)$, $c=3.9167(1)$ Å[a]

h	k	l	$2\theta_{obs}$	I_{obs}	$2\theta_{calc}$	$\Delta 2\theta$	d_{obs}
0	2	0	5.659	3	5.642	0.017	15.60
0	4	0	11.314	3	11.297	0.017	7.814
1	1	0	16.247	1	16.232	0.015	5.451
0	6	0	16.999	5	16.980	0.019	5.212
1	3	0	18.111	1	18.112	−0.001	4.894
1	4	0	19.614	1	19.614	0.000	4.522
1	5	0	21.404	18	21.397	0.007	4.1479
0	8	0	22.727	4	22.706	0.021	3.9094
0	1	1	22.860	6	22.864	−0.004	3.8869
1	6	0	23.399	1	23.400	−0.001	3.7986
0	3	1	24.247	1	24.252	−0.005	3.6677
1	7	0	25.589	1	25.576	0.013	3.4783
0	5	1	26.844	1	26.828	0.016	3.3184
1	8	0	27.902	6	27.890	0.012	3.1949
1	1	1	28.036	6	28.020	0.016	3.1800
0	10	0	28.497	100	28.490	0.007	3.1296
1	3	1	29.174	2	29.180	−0.006	3.0585
1	4	1	30.176	45	30.161	0.015	2.9592
2	0	0	32.284	16	32.285	−0.001	2.7706
1	6	1	32.823	39	32.818	0.005	2.7263
0	12	0	34.365	11	34.348	0.017	2.6074
0	9	1	34.452	12	34.457	−0.005	2.6011
1	11	0	35.426	6	35.430	−0.004	2.5317
1	12	0	38.104	8	38.097	0.007	2.3597
0	11	1	39.110	7	39.094	0.016	2.3013
2	1	1	39.928	14	39.929	−0.001	2.2560
0	14	0	40.300	11	40.302	−0.002	2.2361
2	4	1	41.540	5	41.525	0.015	2.1721
1	11	1	42.491	8	42.484	0.007	2.1257
2	10	0	43.586	24	43.589	−0.003	2.0748
0	13	1	44.114	6	44.111	0.003	2.0512
1	12	1	44.820	10	44.796	0.024	2.0205
2	11	0	45.659	1	45.663	−0.004	1.9853
2	8	1	46.338	28	46.327	0.011	1.9578
1	15	0	46.449	14	46.458	−0.009	1.9534
2	12	0	47.867	13	47.854	0.013	1.8988
2	9	1	47.928	13	47.936	−0.008	1.8965
0	15	1	49.451	3	49.445	0.006	1.8416
1	14	1	49.701	10	49.711	−0.010	1.8329
3	4	0	50.730	1	50.744	−0.014	1.7981
1	5	2	51.563	8	51.563	0.000	1.7710
1	15	1	52.281	2	52.300	−0.019	1.7484
3	6	0	52.520	2	52.514	0.006	1.7409
2	12	1	53.604	1	53.582	0.022	1.7083
1	16	1	54.980	16	54.971	0.009	1.6687
0	10	2	55.280	12	55.286	−0.006	1.6604
3	3	1	55.680	2	55.674	0.006	1.6494
3	4	1	56.260	7	56.260	0.000	1.6338
1	9	2	56.375	4	56.369	0.006	1.6307
2	0	2	57.601	11	57.590	0.011	1.5989
3	6	1	57.896	13	57.913	−0.017	1.5914
1	19	0	58.369	6	58.386	−0.017	1.5797
0	12	2	58.929	3	58.923	0.006	1.5659
3	11	0	59.630	2	59.627	0.003	1.5492
2	17	0	60.297	2	60.302	−0.005	1.5337
1	18	1	60.542	10	60.551	−0.009	1.5281
0	19	1	60.943	2	60.956	−0.013	1.5189
1	20	0	61.502	1	61.513	−0.011	1.5065
2	16	1	62.740	1	62.739	0.001	1.4797
3	10	1	63.028	1	63.018	0.010	1.4736
2	9	2	64.017	1	64.031	−0.014	1.4532
1	21	0	64.686	1	64.703	−0.017	1.4398
2	17	1	65.296	5	65.287	0.009	1.4278
1	14	2	65.503	16	65.507	−0.004	1.4238
3	12	1	66.402	1	66.396	0.007	1.4067
2	11	2	67.086	1	67.080	0.006	1.3940
3	15	0	67.674	6	67.686	−0.012	1.3833
2	12	2	68.787	6	68.802	−0.015	1.3636
1	16	2	70.004	1	70.006	−0.002	1.3429
4	6	0	70.232	1	70.244	−0.012	1.3391
2	13	2	70.655	1	70.651	0.004	1.3321
3	5	2	71.799	1	71.793	0.006	1.3136
0	1	3	72.378	7	72.388	−0.010	1.3046
3	6	2	72.588	3	72.594	−0.006	1.3013
3	7	2	73.554	1	73.537	0.017	1.2866
0	5	3	74.114	1	74.127	−0.013	1.2782
1	0	3	74.627	6	74.625	0.002	1.2707
4	6	1	74.885	4	74.891	−0.006	1.2669
1	4	3	75.772	4	75.773	−0.001	1.2543
3	10	2	77.188	5	77.195	−0.007	1.2348
3	19	0	77.585	4	77.585	0.000	1.2295
4	12	0	78.060	3	78.040	0.020	1.2232
1	24	1	79.228	1	79.253	−0.025	1.2081
4	10	1	79.461	2	79.446	0.015	1.2051
1	9	3	80.383	1	80.384	−0.001	1.1936
4	11	1	80.907	1	80.925	−0.018	1.1872
2	1	3	81.473	3	81.490	−0.017	1.1804
2	23	1	82.662	2	82.678	−0.016	1.1664
2	5	3	83.175	1	83.170	0.005	1.1605
3	14	2	83.970	3	83.951	0.019	1.1515
4	13	1	84.262	1	84.284	−0.022	1.1482
1	12	3	84.794	2	84.793	0.001	1.1424
4	16	0	85.892	3	85.894	−0.002	1.1306
4	2	2	86.133	2	86.139	−0.006	1.1280
2	20	2	87.044	2	87.043	0.001	1.1186
2	10	3	88.391	2	88.390	0.001	1.1049
1	28	0	89.317	2	89.315	0.002	1.0959

Figure of merit: $F_{97}=35.3$ (0.0092, 298) [41].

[a] Electron diffraction indicated that the actual symmetry of this compound is monoclinic, $P2_1/b11$; $a\sim5.5$, $b\sim31$, $c\sim7.8$ Å; $\beta\sim104°$; however, all peaks observed using X-ray powder diffraction could be indexed using the orthorhombic subcell given here.

both *A*- and *B*-sites. The value of a can range from 0 through 0.25, and the b-values can range from 0 to a maximum of 0.38 when $a = 0.25$.[3] The trends in unit cell volume and distortion of the perovskite structure within the single-phase field are consistent with those observed along the boundaries for the $LaMg_{1/2}Ti_{1/2}O_3$–$CaTiO_3$ and La_2O_3–$CaTiO_3$ solid solutions: The least distortion is observed for $LaMg_{1/2}Ti_{1/2}O_3$; the distortion increases slightly and the unit cell volume decreases significantly with increasing $CaTiO_3$ content. Dissolution of La_2O_3 in

[3] The subscripts a and b are related to the formulas given in Fig. 9 for the perovskite solid solutions along the $LaMg_{1/2}Ti_{1/2}O_3$–$CaTiO_3$ and $\frac{1}{2}La_2O_3$–$CaTiO_3$ edges by: $a = x/4$, $b = y/2$.

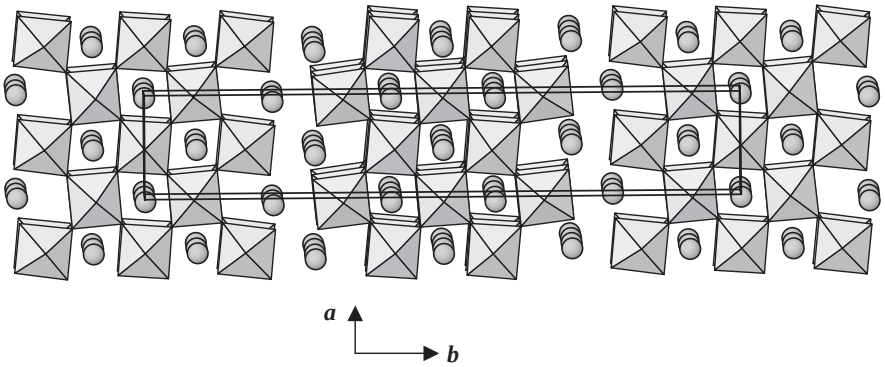

Fig. 4. Suggested crystal structure of $La_{10}MgTi_9O_{34}$ (compound **E**, Table 5), isostructural with $Sr_5TiNb_4O_{17}$, an $n = 5$ member of the "(110) perovskite-slab" homologous series $A_nB_nO_{3n+2}$. The n-value corresponds to the width, in $[BO_6]$ octahedra, of the perovskite slabs, which extend parallel to the parent (110) perovskite planes. The orthorhombic subcells for these homologs exhibit similar a ($\sim$5.5 Å) and c ($\sim$3.9 Å) parameters, and variable b-parameters that reflect slab thickness and translational symmetry. The refined unit cell for $La_9Mg_{0.5}Ti_{8.5}O_{31}$ (compound **F**, Table 6) suggests it is an $n = 4.5$ member of this series, with perovskite slabs alternately 4 and 5 octahedra in width.

$CaTiO_3$ results in expanded unit cell volumes and even larger orthorhombic distortions [37,38]—maxima for both are attained in the endmember composition $La_{0.76}Ca_{0.24}[Ca_{0.38}Ti_{0.62}]O_3$.

Values for relative permittivity (ε) and temperature coefficient of resonant frequency (τ_f, ppm/°C) are included in Fig. 9 for several specimens within the perovskite single-phase region (Table 1) [3,38,56]. For the $LaMg_{1/2}Ti_{1/2}O_3$–$CaTiO_3$ solid solution, τ_f changes sign at 44:56 $LaMg_{1/2}Ti_{1/2}O_3$:$CaTiO_3$ (permittivity 48). For the La_2O_3–$CaTiO_3$ solid solution, $\tau_f = 0$ occurs near 38:62 $1/2La_2O_3$:$CaTiO_3$. As seen in Fig. 9, the dotted line through the perovskite single-phase region connects these two compositions and approximately indicates where single-phase, temperature-stable ($\tau_f = 0$) compositions are expected to form, with relative permittivities of 40–50. As confirmed by measurement (Fig. 9, Table 1), specimens on the $CaTiO_3$ side of the dotted $\tau_f = 0$ line exhibited positive τ_f-values, while those for specimens on the La_2O_3 side were negative.

3.3. $LaMg_{1/2}Ti_{1/2}O_3$–$CaTiO_3$–$La_{0.833}Mg_{0.25}Ti_{0.75}O_3$ system

This ternary section in the quaternary La_2O_3–CaO–MgO–TiO_2 system consists of a single-phase perovskite-like field bounded by the solid solutions $LaMg_{1/2}Ti_{1/2}O_3$–$CaTiO_3$, $LaMg_{1/2}Ti_{1/2}O_3$–$La_{0.833}Mg_{0.25}Ti_{0.75}O_3$ (phase **B**, Fig. 2), and $CaTiO_3$–$La_{0.833}Mg_{0.25}Ti_{0.75}O_3$, as shown in Fig. 10. ($La_{0.833}Mg_{0.25}Ti_{0.75}O_3$ is the endmember of the $(1-x)LaMg_{1/2}Ti_{1/2}O_3$–$xLa_{2/3}TiO_3$ solid solution, $x = 0.5$.) Within the single-phase field, the A-sites of the perovskite structure are occupied by a mixture of La, Ca, and vacancies (□), and the B-sites are occupied by Mg and Ti according to: $La_xCa_y\square_{1-x-y}[Mg_{1.5x+y-1}Ti_{2-1.5x-y}]O_3$, with x or y ranging from 0 through 1. In Fig. 10, the signs of the temperature coefficients of resonant frequency for the components are given in parentheses along with (ε,τ_f) values for the temperature-stable ($\tau_f = 0$) compositions in the $LaMg_{1/2}Ti_{1/2}O_3$–$CaTiO_3$ and $LaMg_{1/2}Ti_{1/2}O_3$–$La_{0.833}Mg_{0.25}Ti_{0.75}O_3$ solid solutions. By joining these points, as shown schematically by the dotted line (Fig. 10), the approximate compositions of perovskite-type phases in this section with $\tau_f = 0$ and permittivities in the 40–50 range can be predicted.

The $LaMg_{1/2}Ti_{1/2}O_3$–$CaTiO_3$–$La_{0.833}Mg_{0.25}Ti_{0.75}O_3$ plane shown in Fig. 10 and the wedge-shaped single-phase perovskite region shown in Fig. 9 are connected by the $LaMg_{1/2}Ti_{1/2}O_3$–$CaTiO_3$ solid solution as a common edge—they comprise two sides of an extensive single-phase perovskite-type volume[4] occurring within the quaternary La_2O_3–CaO–MgO–TiO_2 system (Fig. 11). Therefore, the dotted $\tau_f = 0$ lines in Figs. 9 and 10 (which share a common endpoint at 44:56 LMT:$CaTiO_3$) are traces of a surface that passes through this volume, locating the compositions of an infinite number of $\tau_f = 0$ perovskite-type phases.

4. Conclusions

Subsolidus phase relations have been determined for the La_2O_3–MgO–TiO_2 system and for two ternary sections in the quaternary La_2O_3–CaO–MgO–TiO_2 system. The formation of six ternary phases in the La_2O_3–MgO–TiO_2 system was confirmed. In addition to the previously known compounds $LaMg_{1/2}Ti_{1/2}O_3$, $La_5Mg_{0.5}Ti_{3.5}O_{15}$, and "$La_6MgTi_4O_{18}$", the new phases $La_{10}MgTi_9O_{34}$ and $La_9Mg_{0.5}Ti_{8.5}O_{31}$, and the perovskite-type solid solution $(1-x)LaMg_{1/2}Ti_{1/2}O_3$–

[4] With five currently known vertices: $LaMg_{1/2}Ti_{1/2}O_3$, $CaTiO_3$, $La_{0.833}Mg_{0.25}Ti_{0.75}O_3$ (=50:50 $LaMg_{1/2}Ti_{1/2}O_3$:$La_{2/3}TiO_3$), $La_{0.76}Ca_{0.62}Ti_{0.62}O_3$ (=62:38 $CaTiO_3$:La_2O_3), and $La_{0.64}Ca_{0.04}TiO_3$ (=96:4 $La_{2/3}TiO_3$:$CaTiO_3$).

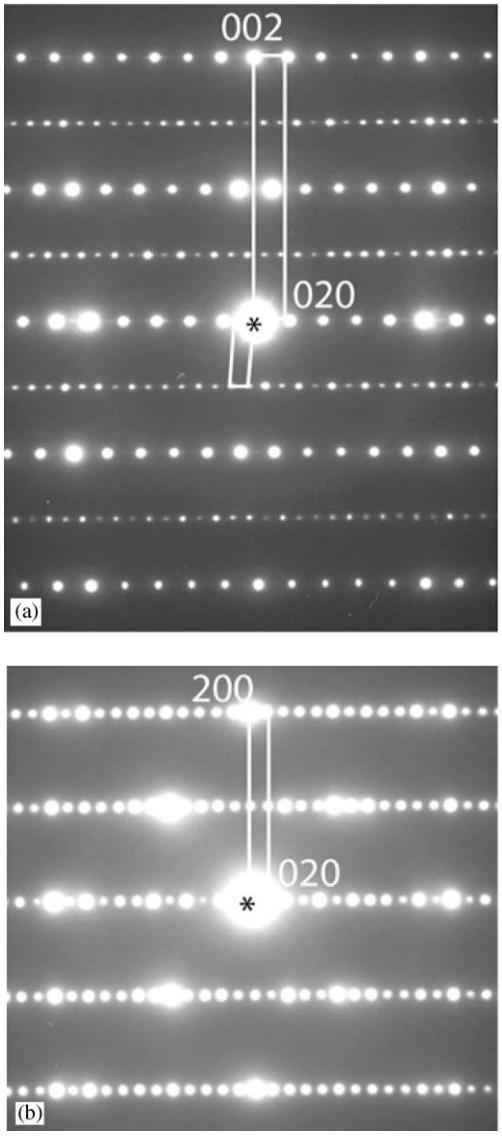

Fig. 5. Selected area electron diffraction patterns for $n=5$ type $La_{10}MgTi_9O_{34}$ in the (a) [100] and (b) [001] directions. The reflections are indexed according to the orthorhombic subcell (Table 6). The superlattice reflections indicating doubling of the c-parameter of the subcell are clearly seen in the [100] orientation. The motif corresponding to the resulting monoclinic superlattice is outlined in (a).

$xLa_{2/3}TiO_3 (0 \leqslant x \leqslant 0.5)$, were found to form. The latter three phases were probably not observed in the previous study of this system [25] because the reaction temperatures (1200°C) and times were insufficient to attain equilibrium. In the present study, the phase previously reported as "$La_6MgTi_4O_{18}$" formed sluggishly as a single phase only when off-composition, at $La_6Mg_{0.913}Ti_{4.04}O_{18}$, suggesting that the formation of *B*-cation vacancies is required for its stabilization. Indexed X-ray powder diffraction patterns are given for $LaMg_{1/2}Ti_{1/2}O_3$, $La_5Mg_{0.5}Ti_{3.5}O_{15}$, $La_6Mg_{0.913}Ti_{4.04}O_{18}$, $La_{10}MgTi_9O_{34}$, and $La_9Mg_{0.5}Ti_{8.5}O_{31}$. All ternary crystal chemistry observed in the La_2O_3–MgO–TiO_2 system is

Table 6
X-ray powder diffraction data for $La_9Mg_{0.5}Ti_{8.5}O_{31}$ (**F**, Fig. 2) n=4.5 member, $A_nB_nO_{3n+2}$ (110) perovskite-slab series; indexed with the orthorhombic subcell: $a=5.5431(2)$, $b=57.055(1)$, $c=3.9123(1)$ Å[a]

h	k	l	$2\theta_{obs}$	I_{obs}	$2\theta_{calc}$	$\Delta 2\theta$	d_{obs}
0	4	0	6.209	2	6.191	0.018	14.22
0	8	0	12.414	3	12.401	0.013	7.124
0	10	0	15.533	3	15.518	0.015	5.700
1	3	0	16.637	1	16.645	−0.008	5.324
1	4	0	17.156	1	17.148	0.008	5.164
1	5	0	17.751	1	17.774	−0.023	4.992
0	12	0	18.652	1	18.647	0.005	4.753
1	8	0	20.281	1	20.274	0.007	4.3750
1	9	0	21.281	19	21.275	0.006	4.1717
0	14	0	21.796	1	21.790	0.006	4.0742
1	10	0	22.349	1	22.343	0.006	3.9747
0	2	1	22.925	6	22.925	0.000	3.8761
1	12	0	24.644	1	24.648	−0.004	3.6095
0	16	0	24.968	1	24.950	0.018	3.5634
1	13	0	25.884	3	25.872	0.012	3.4393
1	14	0	27.130	2	27.136	−0.006	3.2841
0	18	0	28.136	100	28.129	0.007	3.1689
1	5	1	28.997	2	28.986	0.011	3.0768
0	12	1	29.543	5	29.544	−0.001	3.0211
1	7	1	30.010	48	30.004	0.006	2.9752
1	17	0	31.127	11	31.126	0.001	2.8709
0	14	1	31.698	3	31.677	0.021	2.8205
2	0	0	32.284	20	32.273	0.011	2.7706
2	4	0	32.898	40	32.893	0.005	2.7203
0	16	1	33.984	13	33.988	−0.004	2.6358
0	22	0	34.565	5	34.557	0.008	2.5928
1	21	0	36.807	1	36.811	−0.004	2.4399
0	24	0	37.795	1	37.812	−0.017	2.3783
1	22	0	38.268	2	38.284	−0.016	2.3500
0	20	1	39.048	5	39.044	0.004	2.3048
2	2	1	39.961	16	39.957	0.004	2.2543
0	26	0	41.106	10	41.099	0.007	2.1941
1	19	1	41.201	8	41.214	−0.013	2.1892
2	7	1	41.390	2	41.399	−0.009	2.1797
1	20	1	42.441	4	42.436	0.005	2.1281
2	18	0	43.335	19	43.331	0.004	2.0862
2	11	1	43.630	10	43.624	0.006	2.0728
2	19	0	44.439	6	44.445	−0.006	2.0369
0	24	1	44.552	5	44.561	−0.009	2.0320
1	27	0	45.927	7	45.922	0.005	1.9743
0	0	2	46.393	25	46.379	0.014	1.9556
2	16	1	47.581	8	47.572	0.009	1.9095
2	22	0	48.009	10	48.004	0.005	1.8935
1	25	1	49.009	9	49.003	0.006	1.8571
0	28	1	50.462	3	50.456	0.006	1.8070
1	9	2	51.563	8	51.557	0.006	1.7710
1	31	0	52.314	1	52.334	−0.020	1.7473
1	12	2	53.214	2	53.218	−0.004	1.7199
0	30	1	53.543	3	53.531	0.012	1.7101
1	14	2	54.549	2	54.562	−0.013	1.6809
1	29	1	54.743	8	54.741	0.002	1.6754
3	0	1	54.911	6	54.909	0.002	1.6707
0	18	2	55.128	12	55.126	0.002	1.6646
3	6	1	55.828	1	55.823	0.005	1.6454
3	7	1	56.144	7	56.150	−0.006	1.6368
0	32	1	56.701	1	56.689	0.012	1.6221
1	17	2	56.906	4	56.913	−0.007	1.6167
2	0	2	57.617	14	57.629	−0.012	1.5985
1	18	2	57.796	10	57.781	0.015	1.5939
3	11	1	57.946	13	57.942	0.004	1.5902

Table 6
(*continued*)

h	*k*	*l*	$2\theta_{obs}$	I_{obs}	$2\theta_{calc}$	$\Delta 2\theta$	d_{obs}
1	19	2	58.685	1	58.690	−0.005	1.5719
1	35	0	59.013	6	59.014	−0.001	1.5639
0	34	1	59.914	2	59.929	−0.015	1.5426
1	33	1	60.865	9	60.865	0.000	1.5207
0	25	2	62.488	1	62.480	0.008	1.4851
3	19	1	63.689	2	63.686	0.003	1.4599
2	30	1	63.889	2	63.902	−0.013	1.4558
3	20	1	64.601	1	64.592	0.009	1.4415
2	18	2	65.341	18	65.336	0.005	1.4269
0	28	2	66.173	1	66.166	0.007	1.4110
2	32	1	66.742	1	66.752	−0.010	1.4004
1	27	2	67.326	3	67.324	0.002	1.3896
4	0	0	67.528	3	67.539	−0.011	1.3859
4	3	0	67.737	1	67.742	−0.005	1.3822
4	5	0	68.114	1	68.103	0.011	1.3755
2	22	2	68.968	6	68.963	0.005	1.3605
2	34	1	69.708	2	69.721	−0.013	1.3478
4	12	0	70.758	1	70.758	0.000	1.3304
2	38	0	71.385	1	71.390	−0.005	1.3202
3	9	2	71.758	1	71.774	−0.016	1.3143
4	3	1	72.462	1	72.467	−0.005	1.3033
0	44	0	72.884	5	72.887	−0.003	1.2968
0	42	1	73.763	2	73.774	−0.011	1.2835
3	29	1	74.435	6	74.436	−0.001	1.2735
4	18	0	74.696	5	74.695	0.001	1.2697
0	12	3	75.519	2	75.537	−0.018	1.2579
1	7	3	75.764	5	75.773	−0.009	1.2544
3	17	2	76.280	1	76.294	−0.014	1.2472
0	14	3	76.659	1	76.656	0.003	1.2420
0	46	0	76.793	1	76.783	0.010	1.2402
3	18	2	77.048	1	77.045	0.003	1.2367
1	11	3	77.315	4	77.319	−0.004	1.2331
0	16	3	77.960	2	77.941	0.019	1.2245
1	35	2	78.166	5	78.187	−0.021	1.2218
1	44	1	79.745	1	79.740	0.005	1.2015
4	20	1	80.863	1	80.868	−0.005	1.1877
0	46	1	81.301	2	81.308	−0.007	1.1824
2	2	3	81.590	2	81.587	0.003	1.1780
2	44	0	81.962	1	81.965	−0.003	1.1745
0	49	0	82.835	1	82.833	0.002	1.1644
0	40	2	83.881	2	83.879	0.002	1.1525
1	21	3	84.092	2	84.096	−0.004	1.1501
4	25	1	85.604	2	85.601	0.003	1.1336
4	0	2	85.882	1	85.874	0.008	1.1307
4	4	2	86.190	2	86.209	−0.019	1.1274
2	16	3	86.872	1	86.879	−0.007	1.1203
1	25	3	87.934	2	87.949	−0.015	1.1095
3	39	1	88.834	1	88.830	0.004	1.1006
0	43	2	89.095	1	89.091	0.004	1.0980

Figure of merit: $F_{109} = 17.8$ (0.0079, 773) [41].

[a] Electron diffraction indicated that the actual symmetry of this compound is monoclinic, $P2_1/b11.$; $a \sim 5.5$, $b \sim 57$, $c \sim 7.8$ Å; $\beta \sim 98°$; however, all peaks observed using X-ray powder diffraction could be indexed using the orthorhombic subcell given here.

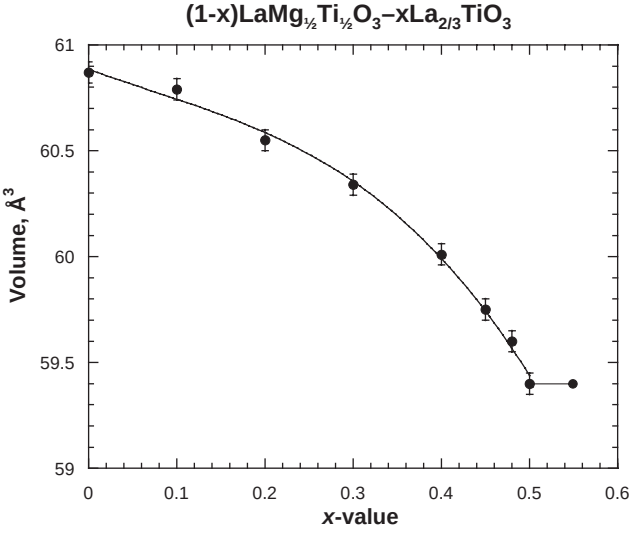

Fig. 6. Pseudo-cubic perovskite unit cell volume vs. x-value for the $(1-x)LaMg_{1/2}Ti_{1/2}O_3$–$xLa_{2/3}TiO_3$ solid solution ($= La_{1-x/3}\square_{x/3}[Mg_{(1-x)/2}Ti_{(1+x)/2}]O_3$, where $\square$ denotes A-site vacancies); the limiting composition occurs at $x = 0.50$. The volumes were calculated from the "(220)"$_{perovskite}$ reflections near 67° 2θ. The number of vacancies formed on the A-sites and the Ti^{4+}/Mg^{2+} ratio on the B-sites both increase with x-value, but have competing effects on volume, resulting in the observed non-linear behavior.

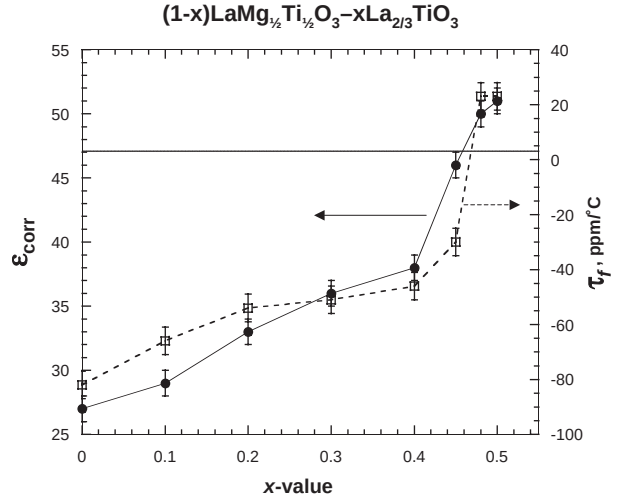

Fig. 7. Relative permittivity (corrected for porosity, ε_{corr}; filled circles) and temperature coefficient of resonant frequency (τ_f, open squares) for the perovskite-related $(1-x)LaMg_{1/2}Ti_{1/2}O_3$–$xLa_{2/3}TiO_3$ solid solution, $0.0 \leqslant x \leqslant 0.50$. With increasing x-value, the permittivity increases and the temperature coefficient becomes more positive, changing sign near $x = 0.47$. The lines connecting the points serve only as guides for the eye. A detailed study of the structural details accompanying these changes in properties is in progress.

dominated by the perovskite structure or derivatives thereof. $LaMg_{1/2}Ti_{1/2}O_3$ was confirmed to exhibit a monoclinic distorted perovskite structure with 1:1 ordering of the B-cations. $La_5Mg_{0.5}Ti_{3.5}O_{15}$ and $La_6Mg_{0.913}Ti_{4.04}O_{18}$ are $n = 5$ and $n = 6$ members, respectively, of the hexagonal series $A_nB_{n-1}O_{3n}$, which features (111)-cut slabs of the perovskite structure separated by layers of ordered B-site vacancies. The new phases $La_{10}MgTi_9O_{34}$ and $La_9Mg_{0.5}Ti_{8.5}O_{31}$ are $n = 5$ and $n = 4.5$ members, respectively, of

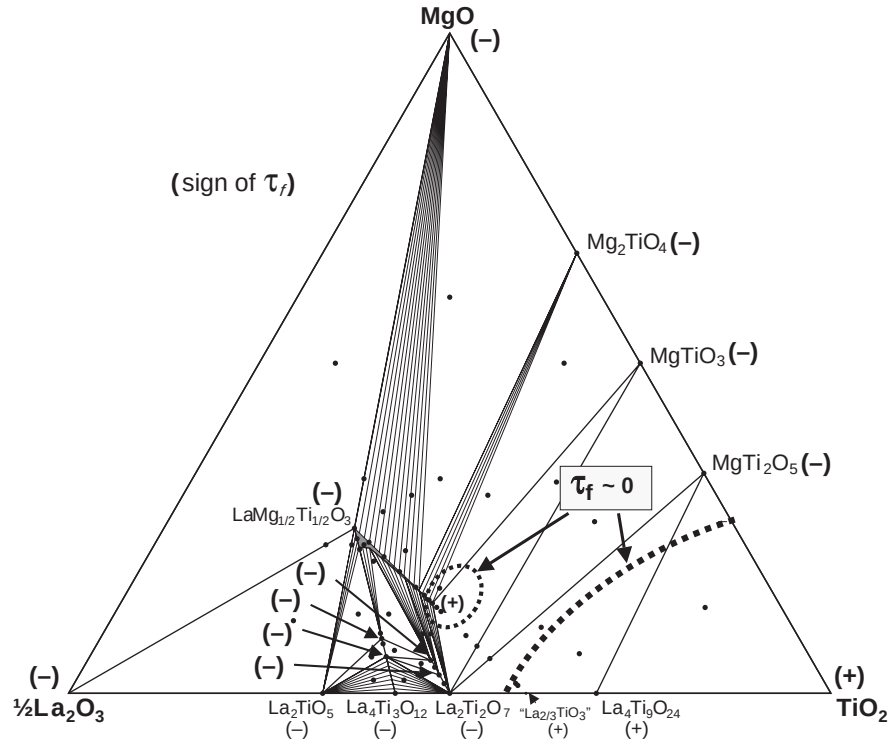

Fig. 8. Subsolidus phase relations in the La_2O_3–MgO–TiO_2 system, sign of the temperature coefficient of resonant frequency (τ_f; in parentheses), and approximate locations of two regions of temperature-stable ($\tau_f = 0$) equilibrium mixtures (dotted lines). Since dielectric properties are additive, a mixture of compounds with opposite signs of temperature coefficients, in some proportion(s), will result in a temperature-stable composition. The curvature of the dotted $\tau_f = 0$ lines is purely schematic.

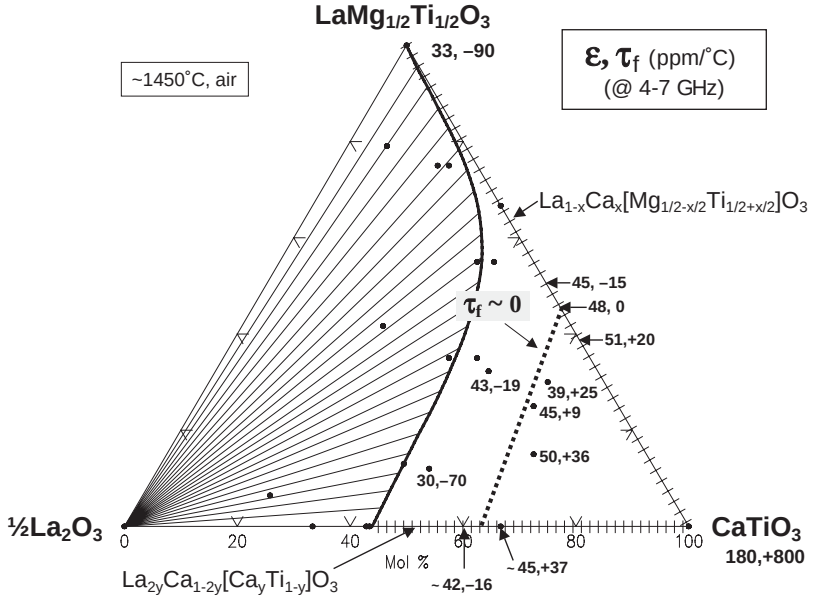

Fig. 9. Subsolidus phase equilibria relations in the $LaMg_{1/2}Ti_{1/2}O_3$–$CaTiO_3$–$\frac{1}{2}La_2O_3$ system as determined in air with synthesis temperatures ~1450°C. This system features a large perovskite-related single-phase field bounded by the complete $LaMg_{1/2}Ti_{1/2}O_3$–$CaTiO_3$ solid solution and the partial solid solution of La_2O_3 in $CaTiO_3$. The formulas for these two solid solutions are shown on the figure. The values for relative permittivity (ε) and temperature coefficient of resonant frequency (τ_f, ppm/°C) are included for a number of specimens. The dotted line, drawn by connecting the $\tau_f = 0$ compositions occurring on the boundaries, schematically indicates where single-phase, temperature-stable ($\tau_f = 0$) perovskite-like compositions are expected to form with permittivities of 40–50.

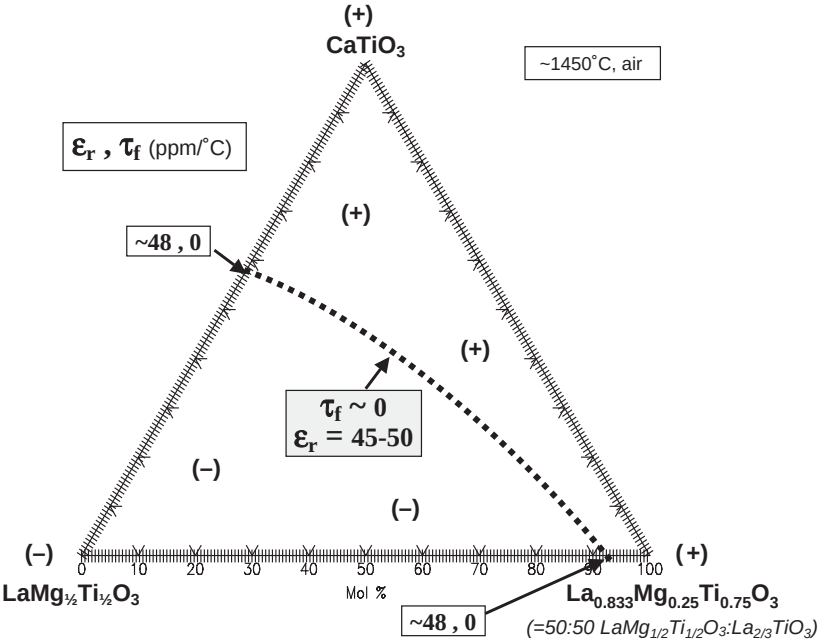

Fig. 10. Subsolidus, single-phase perovskite-like field $LaMg_{1/2}Ti_{1/2}O_3$–$CaTiO_3$–$La_{0.833}Mg_{0.25}Ti_{0.75}O_3$ within the quaternary system La_2O_3–CaO–MgO–TiO_2. The side $LaMg_{1/2}Ti_{1/2}O_3$–$La_{0.833}Mg_{0.25}Ti_{0.75}O_3$ corresponds to the $(1-x)LaMg_{1/2}Ti_{1/2}O_3$–$xLa_{2/3}TiO_3$ solid solution, $0.0 \leqslant x \leqslant 0.50$ (phase **B**, Fig. 2); $La_{0.833}Mg_{0.25}Ti_{0.75}O_3$ corresponds to the limiting composition at $x = 0.5$. Signs of the temperature coefficients of resonant frequency (τ_f) are indicated in parentheses. The sign of τ_f changes from negative to positive in both the $LaMg_{1/2}Ti_{1/2}O_3-La_{2/3}TiO_3$ (Table 1) and $LaMg_{1/2}Ti_{1/2}O_3$–$CaTiO_3$ solid solutions, as indicated on the figure. The connection of these $\tau_f = 0$ points results in the dotted line, which schematically indicates the expected location of single-phase, temperature-stable ($\tau_f = 0$) perovskite-like compositions with permittivities of 45–50.

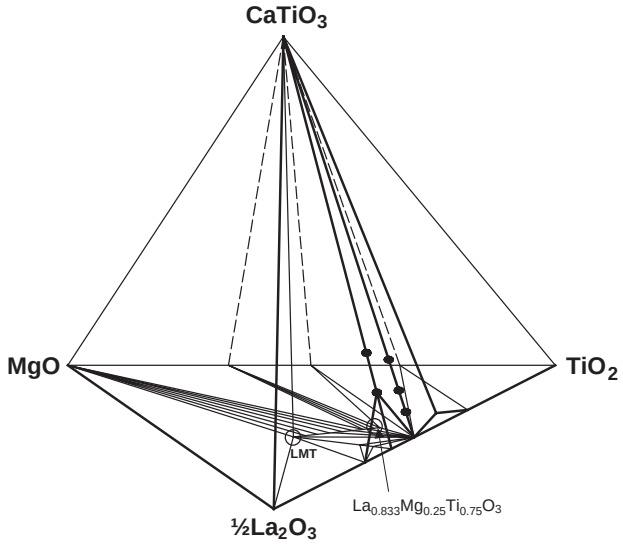

Fig. 11. Quaternary portion of the La_2O_3–CaO–MgO–TiO_2 system showing the locations of the ternary sections shown in Figs. 9 and 10. Compound labels on the sides of the tetrahedron have been omitted for clarity. The base corresponds to the La_2O_3–MgO–TiO_2 system (Fig. 1; LMT = $LaMg_{1/2}Ti_{1/2}O_3$). The plane $CaTiO_3$–LMT–$1/2La_2O_3$ corresponds to the section shown in Fig. 9. The plane $CaTiO_3$–LMT–$La_{0.833}Mg_{0.25}Ti_{0.75}O_3$ corresponds to the section shown in Fig. 10. These two planes are joined by the vertical line $CaTiO_3$–LMT and comprise two sides of an extensive single-phase perovskite-type volume located within the quaternary system. The dotted $\tau_f = 0$ lines in Figs. 9 and 10 (which share a common endpoint at 44:56 LMT:$CaTiO_3$) are traces of a $\tau_f = 0$ surface that passes through this volume, locating the compositions of an infinite number of $\tau_f = 0$ perovskite-type phases.

the orthorhombic (110)-cut perovskite-slab series $A_nB_nO_{3n+2}$. Dielectric property measurements (permittivity and temperature coefficient of resonant frequency, τ_f) mapped onto the phase equilibria relations indicated two regions in the La_2O_3–MgO–TiO_2 system where temperature-stable ($\tau_f = 0$) mixtures or phases can be synthesized. For the $(1-x)LaMg_{1/2}Ti_{1/2}O_3$–$xLa_{2/3}TiO_3$ solid solution, the relative permittivity increases and τ_f becomes more positive with increasing x-value, passing through zero near $x = 0.47$; the changes in properties are accompanied by structural changes which will be described elsewhere.

The phase equilibria results obtained for the ternary La_2O_3–MgO–TiO_2 system, which forms one side of the quaternary La_2O_3–CaO–MgO–TiO_2 system, can be used to project behavior in the higher-order system. For example, the compound $LaMg_{1/2}Ti_{1/2}O_3$ does not occur in equilibrium with the well-known microwave ceramic $MgTiO_3$ (Fig. 1). Therefore, $LaMg_{1/2}Ti_{1/2}O_3$:$CaTiO_3$ solid solutions with permittivities higher than 50 (and which have small positive τ_f values) cannot be temperature-compensated by adding $MgTiO_3$ as a second phase because they will not form a stable phase assemblage: instead, mixtures containing MgO and/or Mg_2TiO_4 will result, as seen by qualitatively extrapolating the fans of two-phase joins from MgO and Mg_2TiO_4 to the $LaMg_{1/2}Ti_{1/2}O_3-La_{2/3}TiO_3$ solid solution (Figs. 1 and 11) into the quaternary system.

Experimental studies of two sections in the quaternary La_2O_3–CaO–MgO–TiO_2 system found that the only phase that forms in the ternary $LaMg_{1/2}Ti_{1/2}O_3$–$CaTiO_3$–La_2O_3 section is an extensive perovskite-type solid solution containing a line of temperature-stable ($\tau_f = 0$) compositions with permittivities in the 40–50 range. Similarly, the entire section $LaMg_{1/2}Ti_{1/2}O_3$–$CaTiO_3$–$La_{0.833}Mg_{0.25}Ti_{0.75}O_3$ consists of a perovskite-type solid solution which also contains a line of temperature-stable ($\tau_f = 0$) compositions with permittivities in the 40–50 range. The lines of $\tau_f = 0$ compositions in these two ternary sections are traces of a surface of $\tau_f = 0$ compositions that passes through an extensive single-phase, perovskite-type volume occurring in the La_2O_3–CaO–MgO–TiO_2 system.

Acknowledgments

The authors appreciate many helpful discussions with R.S. Roth, the assistance of R. Coutts in the preparation of samples, and the efforts of N. Swanson and P.K. Schenck in representation of the phase equilibria data. V.L. Miller was supported by the NSF, DMR program, Research Experiences for Undergraduates (REU).

References

[1] W. Wersing in: B.C.H. Steele (Ed.), Electronic Ceramics, Elsevier Applied Science, New York, 1991 (Chapter 4).
[2] W. Wersing, Curr. Opin. Solid State Mater. Sci. 1 (1996) 715.
[3] T. Negas, G. Yeager, S. Bell, R. Amren, in: P.K. Davies, R.S. Roth (Eds.), Chemistry of Electronic Materials, NIST Spec. Pub. 804, US Government Printing Office, Washington, DC, 20402, 1991, pp. 21–34.
[4] P.K. Davies, in: T. Negas, H. Ling, (Eds.), Materials and Processes for Wireless Communications, American Ceramic Society, Westerville, OH, 1995, pp. 137–151.
[5] R.J. Cava, J. Mater. Chem. 11 (2001) 54.
[6] T.A. Vanderah, Science 298 (2002) 1182.
[7] I. Levin, J.Y. Chan, J.E. Maslar, T.A. Vanderah, S.M. Bell, J. Appl. Phys. 90 (2) (2001) 904 (and references cited therein).
[8] R.C. Kell, A.C. Greenhaum, G.C.E. Olds, J. Am. Ceram. Soc. 56 (1973) 352.
[9] J.B. MacChesney, H.A. Sauer, J. Am. Ceram. Soc. 45 (1962) 416.
[10] N.F. Fedorov, O.V. Mel'nikova, V.A. Saltykova, M.V. Chistyakova, Russ. J. Inorg. Chem. 24 (5) (1979) 649.
[11] M. German, L.M. Kovba, Russ. J. Inorg. Chem. 30 (2) (1985) 176.
[12] S. Skapin, D. Kolar, D. Suvorov, J. Eur. Ceram. Soc. 20 (2000) 1179.
[13] M. Guillen, E.F. Bertaut, C. R. Acad. Sci B Phys. 262 (1966) 962.
[14] P.A. Fuierer, R.E. Newnham, J. Am. Ceram. Soc. 74 (1991) 2876.
[15] M. Nanot, F. Queyroux, J.C. Gilles, A. Carpy, J. Galy, J. Solid State Chem. 11 (1974) 272.
[16] J.P. Guha, D. Kolar, J. Mater. Sci. Lett. 1 (1982) 312.
[17] D. Kolar, S. Gaberscek, B. Volavsek, H.S. Parker, R.S. Roth, J. Solid State Chem. 38 (1981) 158.
[18] N. Huebner, R. Gruehn, Z. Anorg. Allg. Chem. 616 (1992) 86.
[19] M. Abe, K. Uchino, Mater. Res. Bull. 9 (1974) 147.
[20] S. Skapin, D. Kolar, D. Suvorov, J. Am. Ceram. Soc. 76 (9) (1993) 2359.
[21] M. German, L.M. Kovba, Russ. J. Inorg. Chem. 28 (4) (1983) 586.
[22] M. German, L.M. Kovba, Russ. J. Inorg. Chem. 28 (9) (1983) 1349.
[23] M. Avdeev, M.P. Seabra, V.M. Ferreira, J. Mater. Res. 17 (5) (2002) 1112 (and references cited therein).
[24] W.A. Groen, F.P.F. van Berkel, D.J.W. Ijdo, Acta Crystallogr. C 42 (1986) 1472.
[25] Z. Chaogui, W. Shuangyan, L. Fuhui, T. Shujian, L. Guobao, J. Alloys Compd. 289 (1999) 257.
[26] R.L. Shultz, J. Am. Ceram. Soc. 56 (1) (1973) 33.
[27] A.P. Pivovarova, V.I. Strakhov, V.A. Saltykova, Inorg. Mater. 35 (1999) 1288.
[28] I. Naseemabeevi, N.I. Santha, M.T. Sebastian, P. Mohanan, J. Mater. Res. 17 (12) (2002) 3084.
[29] M. Nanot, F. Queyroux, J.C. Gilles, R. Portier, M. Fayard, Mater. Res. Bull. 10 (1975) 313.
[30] M. Nanot, F. Queyroux, J.C. Gilles, J. Solid State Chem. 28 (1979) 137.
[31] M. Nanot, F. Queyroux, J.C. Gilles, J. Solid State Chem. 61 (1986) 315.
[32] M. Nanot, F. Queyroux, J.C. Gilles, J. Solid State Chem. 38 (1981) 74.
[33] A.M. Sych, R.V. Maksakova, I.R. Didukh, Yu.A. Titov, Russ. J. Inorg. Chem. 33 (7) (1988) 1035.
[34] M. German, L.M. Kovba, Russ. J. Inorg. Chem. 30 (8) (1985) 1204.
[35] A.P. Pivovarova, V.I. Strakhov, V.A. Saltykova, Inorg. Mater. 35 (1999) 806.
[36] I. Kim, W. Jung, Y. Inaguma, T. Nakamura, M. Itoh, Mater. Res. Bull. 30 (3) (1995) 307.
[37] V.A. Saltykova, O.V. Mel'nikova, N.F. Fedorov, I.A. Polevaya, Russ. J. Inorg. Chem. 34 (10) (1989) 1520.
[38] I. Molodetsky, L. Farber, P.K. Davies, personal communication.
[39] C.R. Hubbard, Y. Zhang, R.L. McKenzie, Certificate of Analysis, SRM 660, National Institute of Standards and Technology, Gaithersburg, MD, 20899, 1989.
[40] Program CELLSVD by C.K. Lowe-Ma, Naval Air Warfare Center Weapons Division Technical Publication 8128, September 1993.
[41] G.S. Smith, R.L. Snyder, J. Appl. Crystallogr. 12 (1979) 60.
[42] A.C. Larson, R.B. Von Dreele, GSAS - General Structure Analysis System, 1994.
[43] D. Kajfez, P. Guillon, Dielectric Resonators, Artech House, Norwood, MA, 1987, p. 53.
[44] R.G. Geyer, J. Baker-Jarvis, T.A. Vanderah, J. Mantese, in: K.M. Nair, A.S. Bhalla (Eds.), Advances in Dielectric Ceramic Materials, Ceramic Transactions, Vol. 88, The American Ceramic Society, Westerville, OH, pp. 115–128, 1998.
[45] T.A. Vanderah, T.R. Collins, W. Wong-Ng, R.S. Roth, L. Farber, J. Alloys Compd. 346 (2002) 116.
[46] A.R. Drews, W. Wong-Ng, T.A. Vanderah, R.S. Roth, J. Alloys Compd. 255 (1997) 243.
[47] ATOMS for Windows, a computer program to display atomic structures, E. Dowty, Shape Software, Kingsport, TN, 1999, (shape@compuserve.com)
[48] A.R. Drews, W. Wong-Ng, R.S. Roth, T.A. Vanderah, Mats. Res. Bull. 31 (2) (1996) 153.
[49] I. Levin, L.A. Bendersky, Acta Crystallogr. B 55 (6) (1999) 853.
[50] M. Tanaka, H. Sekii, K. Ohi, Japan J. Appl. Phys. 24 (Suppl. 2) (1985) 814.

[51] I. Levin, L.A. Bendersky, T.A. Vanderah, R.S. Roth, O.M. Stafsudd, Mats. Res. Bull. 33 (3) (1998) 501.
[52] R.D. Shannon, Acta Crystallogr. A 32 (1976) 751.
[53] R.G. Geyer, J. Mantese, J. Baker-Jarvis, NIST Technical Note 1371, 1994 (and references cited therein).
[54] D. Kingery, H.K. Bowen, D.R. Uhlmann, Introduction to Ceramics, 2nd Edition, Wiley, New York, 1976 (Chapter 18).
[55] A.E. Paladino, J. Am. Ceram. Soc. (1971) 168.
[56] T. Negas, private communication.